JMEPEG (2010) 19:693–699
DOI: 10.1007/s11665-009-9478-7

1059-9495/$19.00

Film Characteristics of Carbon Steel in Simulant Solution with the Effect of Acetic Acid and CO_2

Z.F. Yin, W.Z. Zhao, W.Y. Lai, C.X. Yin, and S.D. Zhu

(Submitted October 16, 2008; in revised form April 1, 2009)

The work investigated the influence of acetic acid (HAc) on the corrosion behavior of carbon steel exposed to the simulant solution. The analysis methods such as scanning electron microscopy, x-ray diffraction, energy dispersive spectroscopy, and x-ray photoelectron spectroscopy were employed to systematically characterize the morphology and component of the corrosion film. The corrosion rate was calculated by weight loss and electrochemical methods. In addition, the corrosion behavior was further studied by using potentiodynamic polarization and electrochemical impedance spectroscopy. It was shown that the corrosion potential and current density increased with increasing the amounts of HAc. The HAc concentration has an important effect on the corrosion film and the corrosion mechanism.

Keywords acetic acid, corrosion film, electrochemical measurements, XPS

1. Introduction

CO_2 corrosion of carbon steel is a common and very serious problem in the oil industry. It often results in severe damage to pipes and equipment (Ref 1). The understanding of the CO_2 corrosion mechanisms under the influence of an organic acid such as the acetic acid (HAc) has been of great interest to researchers because HAc is an important influence in oilfield environments (Ref 2-6). Crolet et al. (Ref 2) investigated the effect of HAc on the cathodic and anodic charge transfer mechanisms as well as on potential sweeps in the presence of CO_2. The results indicated that the presence of HAc influenced the cathodic limiting current density, but showed an inhibiting effect on the anodic charge transfer mechanism. In addition, within the range of potentials applied, the formation process of corrosion film involves formation and redissolution of corrosion products (Ref 3-5).

When HAc and CO_2 coexist in aqueous solution, both HAc and H_2CO_3 dissociate into hydrogen, acetate, bicarbonate, and carbonate ions

$$HAc \leftrightarrow H^+ + Ac^- \quad \text{(Eq 1)}$$

$$H_2CO_3 \leftrightarrow H^+ + HCO_3^- \quad \text{(Eq 2)}$$

$$HCO_3^- \leftrightarrow H^+ + CO_3^{2-} \quad \text{(Eq 3)}$$

Z.F. Yin, W.Z. Zhao, and **W.Y. Lai**, School of Materials Science and Engineering, Xi'an Jiaotong University, Xi'an, Shannxi 710049, P.R. China; **C.X. Yin**, Tubular Goods Research Center, CNPC, Dianzier Road, Xi'an, Shannxi 710065, P.R. China; and **S.D. Zhu**, School of Materials Science and Engineering, X'an Shiyou University, Xi'an, Shannxi, P.R. China. Contact e-mail: yinzhifu919@sohu.com.

Therefore, HAc is one of the main sources of hydrogen ions when the two acid concentrations are similar. The acetate and carbonate ions form iron acetate and iron carbonate via the following reactions with iron, respectively.

$$Fe + 2Ac^- \rightarrow Fe(Ac)_2 \quad \text{(Eq 4)}$$

$$Fe + CO_3^{2-} \rightarrow FeCO_3 \quad \text{(Eq 5)}$$

As is well known, the solubility of iron acetate is much higher than that of iron carbonate, consequently the corrosion film formation by $Fe(Ac)_2$ does not readily occur. Considering the corrosion films, Johnson and Thomson (Ref 7) found that the most important factors which affect the precipitation of iron carbonate scale are supersaturation and temperature. Earlier work (Ref 8, 9) has shown that in the corrosion system containing HAc, the main cause of carbon steel corrosion is the free HAc and not the acetate ion (Ac^-). Therefore, it is important to determine the relative ratio of free HAc to Ac^- when HAc is present in the corrosion system.

Although iron carbonate film formation mechanisms have been extensively studied using electrochemical techniques or weight loss method (Ref 10-13), the corrosion film formed in the presence of HAc has been scantily characterized. The study aims to investigate the characteristics of surface film, corrosion mechanisms, and electrochemical behavior by using both weight loss and electrochemical techniques, as well as by means of scanning electron microscopy (SEM), x-ray diffraction (XRD), energy dispersive spectroscopy (EDS), and x-ray photoelectron spectroscopy (XPS).

2. Experimental

2.1 Materials and Weight Loss Method

The test material was P110 carbon steel slice with a size of $40 \times 10 \times 3$ mm^3, whose chemical composition was: 0.26 wt.% C, 0.19 wt.% Si, 1.37 wt.% Mn, 0.009 wt.% P, 0.004 wt.% S, 0.148 wt.% Cr, 0.028 wt.% Mo, 0.028 wt.% Ni,

0.019 wt.% Cu, 0.011 wt.% Ti and Fe, balance. Before the corrosion test, the sample was polished on successively finer grades of emery sandpaper up to 800 grit, then degreased with acetone and rinsed with absolute alcohol, weighted using an electronic balance with a precision of 0.1 mg, and put in the high-temperature and high-pressure autoclave (Cortest, USA). Prior to the tests, pure N_2 was bubbled into the simulant solution for 12 h, and then the CO_2 gas was passed into autoclave. The temperature was controlled to be 90 °C and the pressure was maintained at 4 MPa. The corrosion test was carried out for 120 h under static condition. The simulant solution was composed of deionized water and pure chemical agents with a concentration of NaCl 82.4 g/L, Na_2SO_4 2.6 g/L, $NaHCO_3$ 1.1 g/L, $CaCl_2$ 1.3 g/L, and $MgCl_2{\cdot}6H_2O$ 12.6 g/L. In addition, the additional quantities of HAc were 0, 1000, and 5000 ppm, respectively. At least three samples were tested for each experimental condition. After each test, the samples were rinsed with distilled water and ethanol, and then they were divided into two groups: the samples in group one were descaled with Clark solution (20 g Sb_2O_3 + 50 g $SnCl_2$ + 1 L HCl), then the visual observation was done and the weight loss was measured. The samples in group two were not descaled, and were dried and stored in a desiccator until analysis using SEM, XRD, EDS, and XPS.

2.2 SEM, XRD, EDS, and XPS Analysis

Surface film on the corroded sample was analyzed using PHI-5400 ESCA XPS system with a set of experimental parameters as follows: a Mg$K\alpha$ x-ray source with a power of 400 W, a pass energy of 89.450 eV for narrow scan, an analysis area approximately 0.8 mm^2, and a vacuum in the test chamber of 2×10^{-8} Pa. The binding energies (BEs) were calibrated by taking C 1s peak, 284.6 eV as a criterion. XRD experiment was performed by using Japan D/Max-2400 automatic XRD apparatus with Cu$K\alpha$ x-ray source, an accelerating voltage of 40 kV, and a current density of 40 mA/cm^2. SEM and accessory measurement facility of EDS were utilized to investigate surface morphologies of the corrosion film. Before SEM, XRD, EDS, and XPS analyses, the samples were cleaned in acetone in order to remove the surface contamination.

2.3 Electrochemical Method

The electrochemical measurements were conducted by potentiodynamic polarization and electrochemical impedance spectrum (EIS) in a conventional three-electrode cell. The counter electrode was a pair of graphite and the reference electrode a saturated calomel electrode (SCE). All potentials were referred to SCE. An EG&G Princeton Research (PAR) Model 5210 lock-in amplifier and PAR Model 273A potentiostat/galvanostat controlled by a personal computer were used. The EIS measurements were carried out at open-circuit potential using perturbation amplitude of 10 mV. The frequency varied from 100 kHz to 5 mHz. Potentiodynamic polarization was conducted with a sweep rate of 0.5 mV/s. Before experiment, the simulant solution was deaerated by pure N_2 for 1 h and then CO_2 was bubbled in solution for 0.5 h, respectively. Then, different quantities of HAc were poured into the deaerated simulant solution. During the experiments, CO_2 was bubbled successively through the solution. The test temperature was controlled at 90 °C.

3. Results and Discussions

3.1 Weight Loss Experiments

Figure 1 shows the front images of the corrosion films by SEM for P110 carbon steel at 90 °C in simulant solution with different quantities of HAc at 200× magnification. There is obvious evidence of uniform corrosion observed on the corroded samples. In the three experiments, the water chemistry is changing, from an under-saturated iron solution at the beginning to a very super-saturated iron solution at the end of each test. This may create a favorable environment for film formation. The fact is that the crystal grains are bulky, compact, and dense due to the existence of corrosive solution and adequate temperature. In addition, on examination of the SEM images as shown in Fig. 1 we can see that the sizes of the crystals with HAc are greater than those observed without HAc, although both can offer similar protection. Moreover, the sizes of crystals increase with the increase of the amount of HAc. We consider that the addition of HAc increases the crystal nucleation and growth, but the nucleation rate is slower than the growth rate of crystal, which results in the augment of the crystal size. The crystal morphologies show the evidence that the typical oblique hexahedron structure is composed of siderite, i.e., ferrous carbonate ($FeCO_3$), which is confirmed by the analysis of XRD below. Fe^{2+} ions may diffuse into the solution to form the corrosion product $FeCO_3$ when $[Fe^{2+}] \times [CO_3^{2-}]$ exceeds the value of the solubility product of iron carbonate (K_{sp}), iron carbonate precipitates on the steel surface. This is also in accordance with the result by Johnson and Thomson (Ref 7) who found that the most important factors which affect the precipitation of iron carbonate film are supersaturation and temperature.

Figure 2 shows the corrosion rates obtained from weight loss and electrochemical experiments on the P110 carbon steel in simulant solution with different amounts of HAc. It is evident that the corrosion rates measured using the two methods are not in complete agreement, even when HAc is not present. As the HAc concentration increases, the influence of HAc is more pronounced in the case of using electrochemical method. One reason for deviation is attributed to the polarization effect in the electrochemical measurement, which disturbs the sample surface and influences corrosion process. It will become more important when the solution is around saturation point. In addition, the exposure time and CO_2 pressure are the primary reasons to lead to the differences of the corrosion rates. The corrosion films formed on the steel surface in autoclave are different from those formed in the electrochemical cell. Therefore, the corrosion films with different microstructures greatly influence the corrosion rates. In this corrosion system, cathodic polarization consumes H^+ ions and creates locally a higher pH, while the anodic sweep releases more Fe^{2+} ions and increases the Fe^{2+} concentration on the steel surface. Therefore, the increased pH value and Fe^{2+} concentration lead to the high super saturation locally, which speeds up the surface attack, even destroys the formed protective films and then further reacts with the naked substrate. This is in agreement with the viewpoint by Sun et al. (Ref 4). It should be stressed that the corrosion rate at 5000 ppm HAc by electrochemical method is much higher than that using weight loss. This phenomenon can be verified by explanation described above.

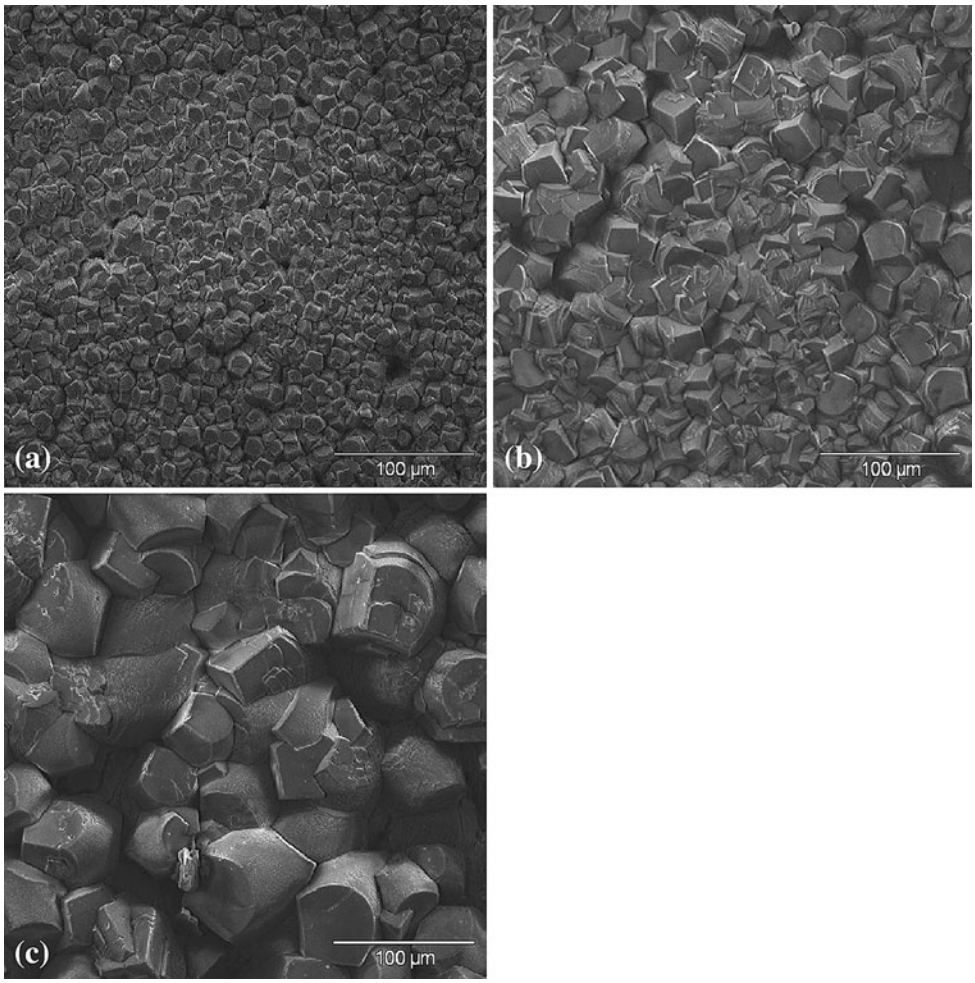

Fig. 1 The SEM images obtained from corrosion film at 90 °C for P110 carbon steel in simulant solution with different quantities of HAc: (a) 0 ppm, (b) 1000 ppm, and (c) 5000 ppm. Magnification 200×

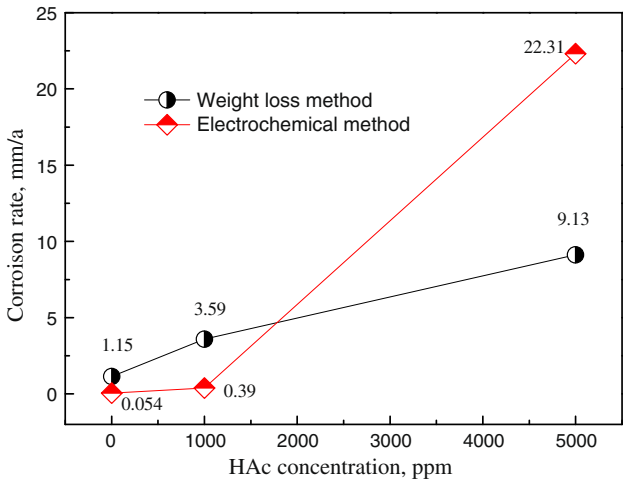

Fig. 2 The corrosion rate obtained from weight loss and electrochemical methods for P110 carbon steel with different quantities of HAc

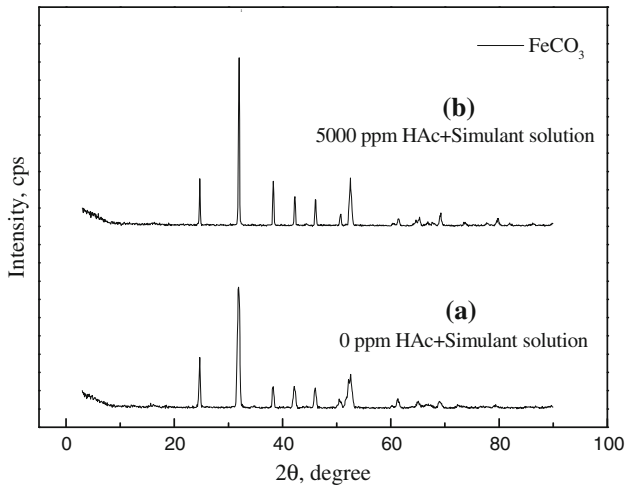

Fig. 3 The XRD spectra obtained from corrosion film at 90 °C for P110 carbon steel in simulant solution with different quantities of HAc: (a) 0 ppm and (b) 5000 ppm

3.2 XRD, EDS, and XPS Analysis

The XRD spectra obtained from corrosion film at 90 °C for P110 carbon steel in simulant solution with the amounts of 0 and 5000 ppm HAc is carried out as shown in Fig. 3. It shows that the corrosion film is indeed composed of siderite ($FeCO_3$) which is the thermodynamically stable corrosion product. As is

known, the solubility of iron acetate is much higher than that of iron carbonate; therefore, the corrosion film formation by $Fe(Ac)_2$ does not readily occur. We can see that the Bragg's angles corresponding to the peak of $FeCO_3$ are similar in the two cases. However, there are some small differences from the XRD results, i.e., 2θ for the 0 ppm HAc case are 24.68°, 31.88°, 38.22°, 42.16°, 46.00°, and 52.56°, in comparison with 2θ for the 5000 ppm HAc case which are 24.70°, 31.96°, 38.30°, 44.44°, 46.10°, and 52.50°. According to Bragg's equation: $2d \sin\theta = \lambda$, where d is the space between the crystal faces and λ is the wavelength of x-ray. The smaller θ implies a bigger space between the crystal faces in lattice as λ is a constant. It can be an evidence for bulky crystals of corrosion film formed at 5000 ppm HAc. However, the extra peak intensities observed at a Bragg's angle of about 32° are obviously different, i.e., the peak intensity becomes higher with the addition of HAc. This result also indicates that the presence of HAc accelerates the corrosion process, which is consistent with SEM analysis.

Figure 4 presents the EDS plots of some elements in corrosion films exposed in simulant solution at 90 °C with different quantities of HAc. It is worth pointing out that the atomic concentrations of both Mg and Ca, which originate in the simulant solution, decrease with the additive amounts of HAc. Conversely, the atomic concentrations of element Fe increase with the increase of HAc. We think that HAc accelerates transfer rate of the species and activates the chemical or electrochemical reactions leading to removal of the deposits involving elements Mg and Ca.

In order to further depict the characteristics of the corrosion films formed on P110 steel in simulant solution with 1000 ppm HAc, XPS spectra and fitting peak spectra are performed as shown in Fig. 5, in which the elements of special interest are iron, oxygen, and carbon. The BEs of these elements in corrosion films are well detected. Figure 5(a) shows survey spectrum of the corrosion film on sample surface. The C 1s high resolution XPS scans in Fig. 5(b) reveal three peaks at the BEs of 284.56, 286.06, and 288.89 eV. The first peak at 284.56 eV close to 284.6 eV corresponds to hydrocarbonate absorbed in corrosion film, while the three peaks at 288.89 around 289.6 eV are attributed to pure iron carbonate (Ref 14). However, the third C 1s peak is the undefined substance due to the complex carbides or imprecise fitting. Figure 5(c) presents the O 1s high resolution XPS spectra of the corrosion film, in which the peaks at BE 529.69, 531.65, and 532.72 eV correspond to $Fe(HCO_3)_2$, $FeCO_3$, and $Fe(OH)_2$ or FeO(OH), respectively. The stronger peak at 531.65 eV is visible near 531.9 eV, which is identified as $FeCO_3$ (Ref 14, 15). However, $Fe(OH)_2$ transformed quickly into FeO(OH) in exposed air environment. The oxides presented in the passive layer should be the substance FeO(OH) which can be explained due to short time exposure in air prior to XPS analysis.

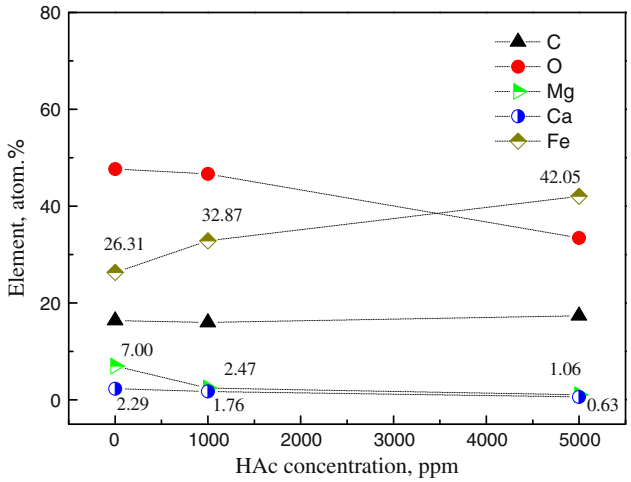

Fig. 4 EDS plots of some elements in corrosion films exposed in simulant solution at 90 °C with different quantities of HAc

An examination of Fe 2p spectra in Fig. 5(d) reveals that the peak at 709.20 eV demonstrates the presence of $FeCO_3$ deposit. In addition, the peak around 713.45 eV may be the characteristics of the Fe^{3+} compound, which may be attributed to the decomposition of $FeCO_3$, in spite of the formation of corrosion film under deoxidized solution. On the other hand, it can be explained considering that the Fe^{3+} compound forms over the exposure of corroded sample to dried atmosphere prior to the XPS analysis. In addition, the XPS peak at 706.40 eV corresponds to Fe^0.

3.3 Electrochemical Measurements

In comparison with weight loss method, potentiodynamic polarization measurements are conducted in simulant solution with different amounts of HAc at 90 °C. The effect of adding HAc, to 1000 and 5000 ppm, on the potentiodynamic sweeps is shown in Fig. 6. As expected, the cathodic limiting current density is shifted to higher current density with an increase in HAc concentration. This is in accordance with the results from Sun et al. (Ref 4) and Wang et al. (Ref 9). However, the anodic branches are virtually unaffected by the addition of HAc, i.e., the mechanism of anode is almost same. In general, the anodic reaction was inhibited with an increase in the HAc concentration, which has been reported by Crolet and Thevenot (Ref 2) and Guo et al. (Ref 16). Since the cathodic charge transfer reaction did not moved significantly with increasing concentrations of HAc, reduction of hydrogen ions more likely occur rather than direct reduction of HAc. It is evident that the corrosion potential (E_{corr}) increases with the amount of HAc, i.e., the corrosion potential shifts to more positive value, as shown in Table 1. The anodic Tafel slopes (b_a) are similar with or without the presence of HAc, while the cathodic branches of the polarization curves almost have the same change trend. In addition, corrosion current density (I_{corr}) increases with the amount of HAc as shown in Table 1. It thus indicates that the corrosion attack increases with increasing the amounts of HAc.

The effect of HAc concentration on the Nyquist plot is shown in Fig. 7(a), as well as the Bode phase angle plots in Fig. 7(b). In the three cases, with an increase in HAc concentration, the intercept of the real axis shifts markedly to lower value. This suggests a big increase in the corrosion rate. The shape of the Nyquist plot corresponding to 0 ppm HAc case includes two depressed semicircles in the high and intermediate frequency regions, respectively. In contrast, the shape of Nyquist plot corresponding to 1000 ppm HAc case includes two capacitive semicircles in the intermediate and low frequency regions, and one inductance arc in the low frequency region. For 5000 ppm HAc case, the Nyquist plot is composed of one capacitive semicircle and two inductance arcs. The depressed semicircle might be due to microscopic surface roughness and presence of a porous corrosion product film as presented by Touzet et al. (Ref 17).

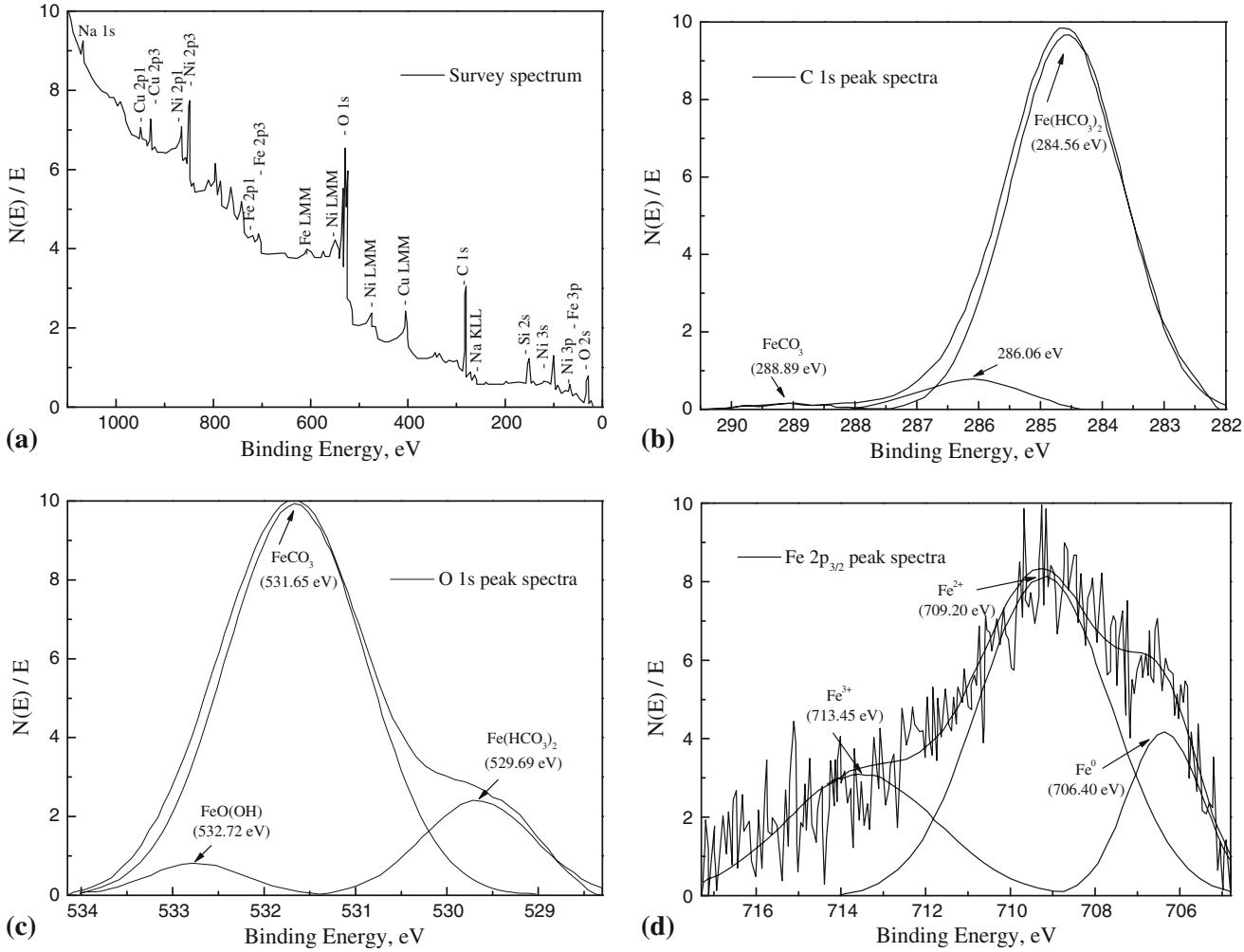

Fig. 5 The XPS fitting spectra obtained from corrosion film at 90 °C for P110 carbon steel with 1000 ppm HAc: (a) survey spectrum of corrosion scale, (b) C 1s characteristic peak, (c) O 1s characteristic peak, and (d) Fe $2p_{3/2}$ characteristic peak

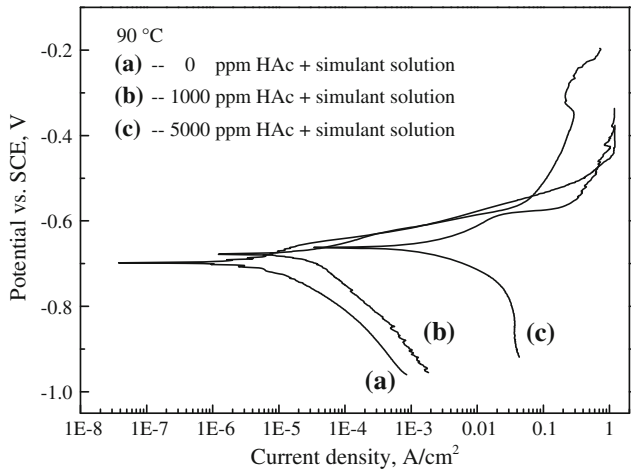

Fig. 6 Potentiodynamic polarization curves obtained on P110 steel in simulant solution with different quantities of HAc: (a) 0 ppm, (b) 1000 ppm, and (c) 5000 ppm

In order to illuminate the relation between corrosion product scale and EIS characteristics, we can assume two variables including the thickness (L) and cover rate (θ) of corrosion scale. According to the present system of electrochemical corrosion, we can verdict that the cover rate of corrosion scale belongs to the case of $0.5 < \theta < 1$. The Faraday current density corresponding to the anodic reaction can be expressed as (Ref 18).

Table 1 Corrosion parameters obtained from potentiodynamic polarization curves at 90 °C in simulant oilfield solution with different quantities of HAc

Parameters	0 ppm	1000 ppm	5000 ppm
E_{corr}, V	−0.695	−0.678	−0.662
b_a, V/dec	0.055	0.047	0.069
b_c, V/dec	−0.071	−0.146	−0.070
I_{corr}, μA/cm^2	4.58	33.3	1900

$$I_F = I_a + I_f \quad \text{(Eq 6)}$$

$$I_a = I_{a1} + I_{a2} = k_1 \cdot c_1^{n_1} \cdot (1-\theta) + k_2 \cdot c_2^{n_2} \cdot (1-\theta) \quad \text{(Eq 7)}$$

$$I_f = i_0 \cdot \exp\left(\frac{b_f \cdot E}{L}\right) \cdot \theta \quad \text{(Eq 8)}$$

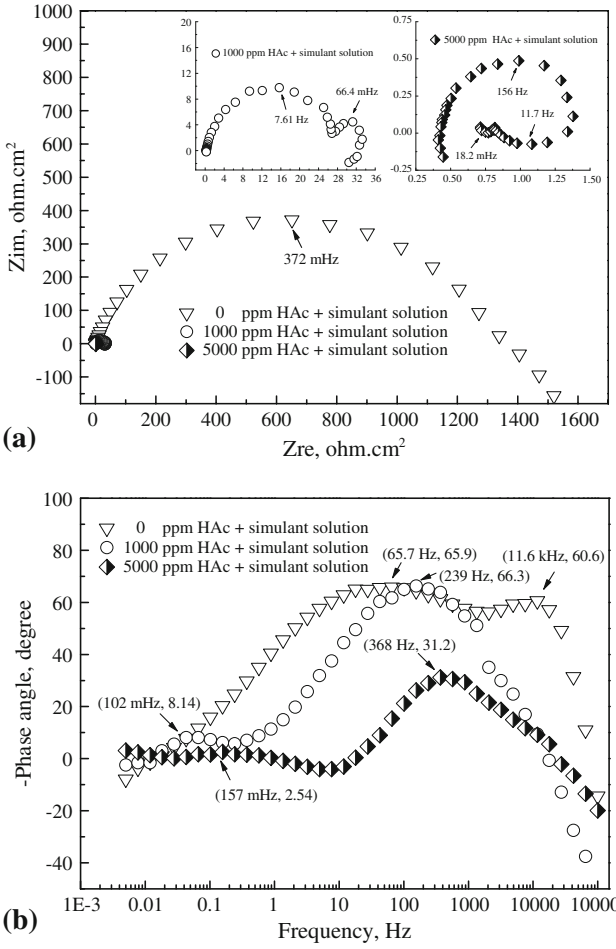

Fig. 7 EIS plots obtained on P110 steel in simulant solution with different quantities of HAc: (a) Nyquist plots and (b) Bode phase angle plots

$$b_f = \alpha \cdot n_f \cdot d/RT \quad \text{(Eq 9)}$$

where the current densities of I_{a1} and I_{a2} in regions are calculated by Eq 4 and 5, respectively. c_1, c_2, n_1, and n_2 are the concentrations of Ac^- and CO_3^{2-}, reaction orders, respectively. I_f denotes the current density in corrosion scale region, d denotes ion transfer distance, and n_f denotes charge number of transfer ion.

The corrosion film dissolves into the solution to maintain the reaction equilibrium. We can assume that I_d is the total dissolving current densities of $Fe(Ac)_2$ and $FeCO_3$, while I_{d1} and I_{d2} are the dissolving current densities which are induced by reduction of the thickness (L) and cover rate (θ) of corrosion scale, which can be described as follows (Ref 19):

$$I_d = nF\nu\theta \quad \text{(Eq 10)}$$

Therefore, the Faraday admittance based on the investigation by Cao (Ref 20) can be expressed as

$$Y_F = \frac{1}{R_t} + \frac{A(D-\omega^2)+\omega^2 BT}{(D-\omega^2)+\omega^2 T^2} + j\omega\frac{BD-AT-\omega^2 B}{(D-\omega^2)+\omega^2 T^2} \quad \text{(Eq 11)}$$

where

$$\frac{1}{R_t} = \left(\frac{\partial I_F}{\partial E}\right)_{ss} \quad \text{(Eq 12)}$$

$$A = m_2 b_1 J_{21} - m_1 b_1 J_{22} - m_2 b_2 J_{11} \quad \text{(Eq 13)}$$

$$B = m_1 b_1 + m_2 b_2 \quad \text{(Eq 14)}$$

Then,

$$m_1 = \left(\frac{\partial I_F}{\partial \theta}\right)_{ss} = \left(\frac{\partial (I_a + I_f)}{\partial \theta}\right)_{ss} = \frac{I_f}{\theta} - \frac{I_a}{1-\theta} < 0$$

$$m_2 = \left(\frac{\partial I_F}{\partial L}\right)_{ss} = \left(\frac{\partial (I_a + I_f)}{\partial L}\right)_{ss} = I_s \cdot \left(\frac{-b_s E}{L^2}\right) < 0$$

$$J_{11} = \frac{\partial \theta'}{\partial \theta} = -K_1\left(\frac{I_{a1}+I_{a2}}{1-\theta} + \frac{I_{d1}}{\theta}\right) < 0$$

$$J_{21} = \frac{\partial L'}{\partial \theta} = K_2(I_f - I_{d2})/\theta > 0$$

$$J_{22} = \frac{\partial L'}{\partial L} = K_2 I_f\left(\frac{-b_s \cdot E}{L^2}\right) < 0$$

$$b_1 = \frac{\partial \theta'}{\partial E} = K_1\left(\frac{\partial I_{a1} + \partial I_{a2}}{\partial E} - \frac{\partial I_{d1}}{\partial E}\right) = K_1\left(\frac{1}{R_1} - \frac{1}{R_{d1}}\right)$$

$$b_1 = \frac{\partial L'}{\partial E} = K_2\left(\frac{\partial I_f}{\partial E} - \frac{\partial I_{d2}}{\partial E}\right) = K_2\left(\frac{1}{R_f} - \frac{1}{R_{d2}}\right)$$

where the subscript ss denotes the stationary state, K_1 and K_2 denote transfer coefficient. Therefore, $D = J_{11} \cdot J_{22} > 0$, $T = -(J_{11} + J_{22}) > 0$ and $T^2 \geq 4D$, the system meets the stabilization condition of the stationary state. When $b_1 > 0$ and $b_2 < 0$, there exists capacitance arcs and inductance arc in Nyquist plots. In the present system, the sample surface has steady corrosion scale region and active region. As cover rate (θ) of corrosion scale increases, the inductance arc gradually becomes smaller while capacitance arc gradually becomes larger in low frequency region. Based on this overview, the Nyquist plot reflects this characteristics and HAc indeed has an activation role in CO_2 corrosion.

4. Conclusions

The corrosion films have uniform, compact, and dense microstructures. The sizes of crystals increase with the increase of the amount of HAc. It is evident that the corrosion rates measured using both weight loss and electrochemical methods are not in complete agreement, even when HAc is not present. The corrosion film is mainly composed of siderite ($FeCO_3$). Moreover, XPS depth profiles show the BEs of iron, oxygen, and carbon elements in corrosion film. In addition, the cathodic limiting current density is shifted to higher current density with an increase in HAc concentration. The corrosion potential shifts to more positive value as HAc increase. As cover rate (θ) of corrosion film increases, the inductance arc gradually becomes smaller while capacitance arc gradually becomes larger in low frequency region.

Acknowledgment

The authors want to thank the Key Laboratory Opening Fund (No. 06A40302) of Corrosion and Protection of Tabular Goods

Research Center of China National Petroleum Corporation for supports to this work.

References

1. C. de Waard, U. Lotz, and D.E. Milliams, Predictive Model for CO_2 Corrosion Engineering in Wet Natural Gas Pipelines, *Corrosion*, 1991, **47**(12), p 976–985
2. J.L. Crolet, N. Thevenot, and A. Dugstad, Role of Free Acetic Acid on the CO_2 Corrosion of Steels, *Corrosion*/99, NACE International, Houston, TX, 1999, paper no. 24
3. K.A. Christiansen, H. Hoeg, K. Michelsen, G. Bech-Nielsen, and H. Nord, Anodic Dissolution of Iron. I. General Mechanism, *Acta Chem. Scand.*, 1961, **15**, p 300–320
4. Y. Sun, K. George, and S. Nesic, The Effect of Cl^- and Acetic Acid on Localized CO_2 Corrosion in Wet Gas Flow, *Corrosion*/03, NACE International, Houston, TX, 2003, paper no. 327
5. H. Nord and G. Bech-Nielsen, The Anodic Dissolution of Iron-III. Coverage on Iron in the Active and Passive States in Acid Carboxylate Solutions, *Electrochim. Acta*, 1971, **16**, p 849–864
6. B. Hedges and L. McVeigh, The Role of Acetate in CO_2 Corrosion: The Double Whammy, *Corrosion*/99, NACE International, Houston, TX, 1999, paper no. 21
7. M.L. Johnson and M.B. Thomson, Ferrous Carbonate Precipitation Kinetics and its Impact on CO_2 Corrosion, *Corrosion*/91, NACE International, Houston, TX, 1991, paper no. 268
8. K. George, S. Nesic, and C. de Waard, Electrochemical Investigation and Modeling of Carbon Dioxide Corrosion of Carbon Steel in the Presence of Acetic Acid, *Corrosion*/04, NACE International, Houston, TX, 2004, paper no. 379
9. S. Wang, K. George, and S. Nesic, High Pressure CO_2 Corrosion Electrochemistry and the Effect of Acetic Acid, *Corrosion*/04, NACE International, Houston, TX, 2004, paper no. 375
10. I. Sekine and K. Senoo, The Corrosion Behaviour of SS 41 Steel in Formic and Acetic Acids, *Corros. Sci.*, 1984, **24**(5), p 439–448
11. I. Sekine, S. Hatakeyama, and Y. Nakazawa, Effect of Water Content on the Corrosion Behaviour of Type 430 Stainless Steel in Formic and Acetic Acids, *Electrochim. Acta*, 1987, **32**(6), p 915–920
12. A. Dugstad, The Importance of $FeCO_3$ Supersaturation on the CO_2 Corrosion of Carbon Steels, *Corrosion*/92, NACE International, Houston, TX, 1992, paper no. 14
13. M.M. Singh and A. Gupta, Corrosion Behavior of Mild Steel in Acetic Acid Solutions, *Corrosion*, 2000, **56**(4), p 371–379
14. J.K. Heuer and J.F. Stubbins, An XPS Characterization of $FeCO_3$ Films from CO_2 Corrosion, *Corros. Sci.*, 1999, **41**(7), p 1231–1243
15. Z.F. Yin, W.Z. Zhao, Z.Q. Bai, and Y.R. Feng, Characteristics of CO_2 Corrosion Scale Formed on P110 Steel in Simulant Solution with Saturated CO_2, *Surf. Interf. Anal.*, 2008, **40**, p 1231–1236
16. X.P. Guo, Z.Y. Chen, D. Liu, K. Bando, and Y. Tomoe, The Effect of Acetic Acid Acetate on CO_2 Corrosion on Carbon Steel, *Corrosion*/05, NACE International, Houston, TX, 2005, paper no. 306
17. M. Touzet, M. Cid, M. Puiggali, and M.C. Petit, An EIS Study and Auger Analysis on 304L Stainless Steel in Hot Chloride Media before and after a Sample Straining, *Corros. Sci.*, 1993, **34**(7), p 1187–1196
18. C.N. Cao, J. Wang, and H.C. Lin, Feature of AC Impedance of Pitting Corroded Electrodes during Pits Propagation, *J. Chin. Soc. Corros. Prot.*, 1989, **9**(4), p 261–270
19. D.H. Davies and G.T. Burstein, The Effects of Bicarbonate on the Corrosion and Passivation of Iron, *Corrosion*, 1980, **36**(8), p 416–422
20. C.N. Cao, On the Impedance Plane Displays for Irreversible Electrode Reactions Based on the Stability Conditions of the Steady-State II. Two State Variables besides Electrode Potential, *Electrochim. Acta*, 1990, **35**(5), p 837–844